# Thermal expansion and electrical conductivity of Fe and Cu doped $MnCo_2O_4$ spinel

Belma Talic[a,b], Peter Vang Hendriksen[b], Kjell Wiik[a], Hilde Lea Lein[a]

[a]*Department of Materials Science and Engineering, Norwegian University of Science and Technology*
[b]*Department of Energy Conversion and Storage, Technical University of Denmark*

**Abstract.** Manganese cobalt spinel oxides are promising coating materials for corrosion protection of metallic interconnects in solid oxide fuel cell stacks. This work investigates how Fe and Cu doping affect the crystal structure, thermal expansion and electrical conductivity of the $MnCo_{2-x}M_xO_4$ (M=Cu, Fe; x = 0.1, 0.3, 0.5) spinel oxides. Single phase cubic spinels were successfully prepared by spray pyrolysis. The electrical conductivity between room temperature and 1000 °C increased with addition of Cu and decreased with addition of Fe. The thermal expansion coefficient (TEC) between 50 and 800 °C decreased from 14.4 to $11.0\times10^{-6}$ $K^{-1}$ going from $MnCo_2O_4$ to $MnCo_{1.5}Fe_{0.5}O_4$. The TEC of the Cu substituted materials did not follow any obvious trend with composition and was likely influenced by precipitation of CuO during heating. Based on their physical properties, the Fe doped materials are the most attractive for application as SOFC interconnect coatings.

Keywords: Solid oxide fuel cell; thermal expansion; electrical conductivity; spinel

## 1. Introduction

The lifetime and performance of solid oxide fuel cell (SOFC) stacks is today among other factors limited by degradation of the ferritic stainless steel (FSS) interconnect [1,2]. Under SOFC operating conditions the FSS is oxidized to form a continuous scale, typically composed of $Cr_2O_3$ and $MnCr_2O_4$ [3]. Due to the modest electrical conductivity of these materials [4,5], the resistance across the stack increases with time as the oxide scale grows thicker [6]. An additional challenge is the vaporization of Cr(VI) species from the scale surface by reaction with oxygen and water vapor present on the cathode side of the SOFC [7,8]. The volatile Cr(VI) species deposit on electrochemically active sites of the cathode, thereby causing significant performance degradation [9–11]. To mitigate these issues, the FSS may be coated with a protective material.

The protective coating should have a sufficiently high electrical conductivity, a thermal expansion coefficient (TEC) matching the FSS interconnect and other SOFC materials, and a low oxygen and chromium diffusion coefficient to limit growth of the oxide scale and vaporization of Cr(VI) [12]. The TEC target will be dictated by the thickest layer in the SOFC stack, which depends on the specific stack design. For a Ni-YSZ anode supported cell the TEC target will be $12.5\times10^{-6}$ $K^{-1}$ while for an YSZ electrolyte supported cell the target will be $10.9\times10^{-6}$ $K^{-1}$ (for the temperature range 25-900 °C) [13]. The TEC of Crofer 22 APU, a FSS commonly used as the interconnect material is $12.3\times10^{-6}$ $K^{-1}$ (25-900 °C) [14].

Several materials have been investigated as protective coatings for SOFC interconnects, including rare-earth oxides [15,16] and various lanthanum-based perovskites [17–19]. $(Mn,Co)_3O_4$ spinel oxides were first suggested as a coating material candidate by Larring and Norby [20], and have received increasing attention over the last decade [21–28]. The most widely studied compositions in this system are $Mn_{1.5}Co_{1.5}O_4$ and $MnCo_2O_4$. Although these materials are not stable under the reducing conditions found on the anode side of the SOFC, they are considered promising coatings for the cathode side, where they limit Cr-volatilization and reduce the oxidation rate of the FSS [29–31].

The $AB_2O_4$ spinel structure (space group *Fd-3m*) adopted by $MnCo_2O_4$ can be described as a cubic close packed arrangement of oxygen ions where 1/8 of the available tetrahedral sites and 1/2 available octahedral sites are occupied by cations. The spinel structure is very flexible in terms of site occupancy and oxidation states of the elements, which makes characterization of the cation distribution complicated when transition metal cations are involved. Several suggestions for the cation

distribution in $MnCo_2O_4$ have been put forth [32–39]. Most of these agree that tetrahedral sites primarily are occupied by $Co^{2+}$, while there is more debate about the oxidation states of Mn and Co occupying the octahedral sites. It was early shown by Yamamoto et al. [32] that the lattice parameter of $MnCo_2O_4$ is lower when synthesized by a low-temperature (80 °C) method compared to when synthesized by solid-state reaction at 1000 °C. At the time, this was attributed to a higher fraction of the tetrahedral sites being occupied by $Mn^{2+}$ when the material is prepared at a low temperature. More recently it has been shown that preparation of $MnCo_2O_4$ below ca. 500-600°C yields a cation deficient spinel having a smaller lattice parameter compared to the stoichiometric material [34,40–44]. For convenience, the cation deficiency is often designated as an excess of oxygen, i.e. $MnCo_2O_{4+\delta}$, with $\delta$ up to 0.6 reported [40]. Upon heating above ca. 500-700 °C oxygen is released to form stoichiometric $MnCo_2O_4$ [40]. There are no reports about the process being reversible, i.e. that oxygen is taken up during cooling.

The small polaron hopping mechanism is generally accepted as the mechanism for electrical conductivity in spinel oxides containing transition metal cations [45,46]. Since the distance between octahedral sites is shorter than the distance between tetrahedral sites in the spinel structure, hopping takes place primarily between multivalent cations on the former [45]. For $MnCo_2O_4$, hopping is believed to take place mainly between $Mn^{3+}/Mn^{4+}$ pairs on the octahedral sites, with a possible contribution due to hopping between $Co^{2+}/Co^{3+}$ pairs [47,48]. There is considerable scatter in literature regarding the magnitude of the electrical conductivity in this material, with values measured in air at 800 °C ranging from 34 to 132 S/cm [49–53]. There is also scatter in the reported thermal expansion coefficient of $MnCo_2O_4$, ranging from 9.7-13.5×$10^{-6}$ $K^{-1}$ between room temperature and 800 °C [49–51,53,54].

There have been several attempts to improve the electrical conductivity and tailor the thermal expansion behavior of the $(Mn,Co)_3O_4$ spinels by partially substituting Co with Ti [55], Ni [56], Fe [57,58], Cu [59–62] or Bi [63]. There is consensus that doping with Cu increases both the electrical conductivity and the thermal expansion coefficient [60–62]. It has also been reported that Cu-doping lowers the sintering temperature relative to $(Mn,Co)_3O_4$ [56,58,59]. It is however not clear in all of the cases how doping affects the electrical conductivity and thermal expansion coefficient of $(Mn,Co)_3O_4$ spinels. For example, addition of Fe is reported to both increase [57] and decrease [51] the electrical conductivity.

The aim of this work is obtain better understanding of the electrical and thermal behavior of the spinel oxides by providing a thorough characterization of these properties in $MnCo_{2-x}M_xO_4$ (M=Cu, Fe; x = 0.1, 0.3, 0.5). Iron and copper were chosen as substitutional elements based on an investigation of several binary spinels made by Petric and Ling [53], where it was shown that copper spinels exhibit appreciable electrical conductivities while ferrite spinels typically have TEC in the range of 11-12×$10^{-6}$ $K^{-1}$, thus providing a good match with other SOFC components.

## 2. Experimental

### 2.1 Powder synthesis

$MnCo_{2-x}M_xO_4$ (M=Cu, Fe; x = 0, 0.1, 0.3, 0.5) powders were synthesized by spray pyrolysis using pilot-scale equipment. The details of this synthesis method have been described by Mokkelbost et al. [64]. Precursor solutions were prepared by dissolving metal nitrates, $Mn(NO_3)_2{\times}H_2O$ (98 %, Aldrich), $Co(NO_3)_2{\times}6H_2O$ (97.7 % min., Alfa Aesar), $Fe(NO_3)_3{\times}9H_2O$ (> 98 %, Alfa Aesar) and $Cu(NO_3)_2{\times}2.5H_2O$ (Rectapur, VWR), in distilled water by stirring overnight. The precursor solutions were filtered and their exact concentrations determined by thermogravimetrical analysis of the weight change after heating to 800 °C. They were then mixed in stoichiometric amounts according to the target compositions (Table 1) and stirred overnight. The mixed solutions were atomized by spraying through a two-phase nozzle at a rate of 10 L/h into a rotating furnace set to a target temperature of 1000 °C. The high temperature causes the atomized droplets to decompose instantly, forming the oxides. The resulting powders were collected at the furnace outlet and calcined in air at 650 °C for 10 h to decompose any remaining organics. The heating and cooling rate (HCR) during calcination

was 200 °C/h. The powders were subsequently ball milled overnight in 100 % ethanol (250 ml PE-bottles, Ø 10 mm YSZ milling balls), dried in a rotavapor, and sieved (250 μm).

The calcined (650 °C) powders were used for structural and thermogravimetric analysis. For measurement of the electrical conductivity and thermal expansion coefficient, the powders were pressed into bars/pellets and sintered in air at 1050 °C or at 1100 °C+800 °C, respectively. Details about the two sintering procedures are given in the following.

**Table 1:** Target compositions of prepared spinel powders and abbreviations used throughout this text.

| Composition | Abbr. |
|---|---|
| $MnCo_2O_4$ | MC |
| $MnCo_{1.9}Fe_{0.1}O_4$ | Fe1 |
| $MnCo_{1.7}Fe_{0.3}O_4$ | Fe3 |
| $MnCo_{1.5}Fe_{0.5}O_4$ | Fe5 |
| $MnCo_{1.9}Cu_{0.1}O_4$ | Cu1 |
| $MnCo_{1.7}Cu_{0.3}O_4$ | Cu3 |
| $MnCo_{1.5}Cu_{0.5}O_4$ | Cu5 |

### 2.2 Characterization

Structural characterization was performed on a Bruker DaVinchi X-ray diffractometer (XRD) with Cu-Kα radiation. Powder samples were mixed with ethanol and applied to a silicon single crystal sample holder while solid samples were mounted in a large-cavity sample holder using molding clay. The diffractograms were recorded on rotating samples from 15-75° 2θ using a step size of 0.02° and a collection time of 1 s per step. Lattice parameters were refined by structure fitting of the diffraction patterns (Pawley method) using Topas software (Bruker).

Thermal expansion was characterized in a Netzsch DIL 402C dilatometer from 30-1000°C and reverse (HCR: 2 °C/min) under flowing (30 ml/min) synthetic air. All measurements were corrected against an $Al_2O_3$ standard. Dense pellets for the measurement were prepared by uniaxial pressing of the spinel powders in a Ø=5 mm steel die, sintering in air at 1100 °C for 5 h and subsequently annealing in air at 800 °C for 12 h (HCR: 2 °C/min). The annealing step was included to re-oxidize the spinel, which is partially decomposed when heated above 1050 °C in air [39,65]. The pellet ends were ground with #1200 SiC paper to make the surface planes parallel. Final pellet length was 8-11 mm. XRD was used to confirm that all materials were phase pure cubic spinels after the sintering procedure. For this purpose, larger pellets (Ø 20 mm) were prepared and sintered following the above described procedure. Before characterization, the pellets were ground with #500 SiC paper to remove 1-2 mm of the surface layer.

Thermogravimetric analysis (TGA) was performed using a TG 439 Thermo-Microbalance from Netzsch. The equipment consists of an electrically compensating symmetrical balance with two separate ovens for the sample and a counter weight, operating at identical heating and flow rates. The equipment has a resolution of 0.1 μm. Analysis was performed on ca. 15 mg of spinel powder with ca. 9.9 mg $Al_2O_3$ powder as the counter weight. Alumina crucibles containing the powders were suspended from the weighing beam using Pt30%Rh wires. The mass change was recorded between room temperature and 800 °C in flowing air (10 ml/min) at various heating and cooling rates. A background correction was made for each temperature program by measuring with empty alumina crucibles. In theory, buoyancy effects should be eliminated by the experimental set-up, however, a small influence was detected in the background measurement. The background data are provided in the Supplementary Material (Figure S1). After correcting for the background, the experimental results were fitted to a polynomial curve to reduce noise inherent to the measurement and improve readability of the figures. Details about the noise reduction procedure and the original data may be found in the Supplementary Material (Figure S2).

Electrical conductivity was characterized by the four-probe method on sintered rectangular bars. The bars were made by uniaxial pressing of the spinel powders in a steel die and sintering in air at

1050 °C for 5 h (HCR: 2 °C/min). The edges of the bar were cut to dimension (ca. 4×6×18 $mm^3$) using a diamond saw and lightly ground with #1200 SiC-paper. Pt-wires were attached to the sides of the bars, which were painted with Pt-paste and then heat treated at 1000 °C for ca. 10 min in air (HCR: 2 °C/min) to ensure good electrical contact. The electrical conductivity was measured in flowing air between room temperature and 1000 °C with 1 h dwell time for each 100 °C (HCR: 1 °C/min). Temperature was monitored by a S-type thermocouple placed close to the sample surface. Current was supplied by a Keithley 580 micro-ohmmeter and varied between 10-100 mA depending on the resistance. The current direction was switched at a frequency of ca. 1 Hz and the average of the measured resistance in forward and reverse directions of passing current was used in order to eliminate any thermoelectric emf. The resistance was recorded every 10 min throughout the measurement. The measured resistance was used to calculate the electrical conductivity according to:

$$\sigma_m = \frac{1}{R} \cdot \frac{L}{A} \tag{1}$$

where $R$ is the resistance [Ω], $L$ is the distance between the voltage probes [cm] and $A$ is the cross sectional area of the sample bar [$cm^2$]. The Bruggeman asymmetric model was used to correct the measured electrical conductivity for sample porosity according to [66,67]:

$$\sigma = \sigma_m \cdot \frac{1}{(1-p)^{\frac{3}{2}}} \tag{2}$$

where $\sigma$ is the corrected conductivity, $\sigma_m$ is the measured conductivity and $p$ is the sample pore fraction. The porosity was determined by the Archimedes method according to ISO 5017:1998(E) using isopropanol as the solvent. The theoretical density of the spinel oxides was calculated using XRD results for the calcined powders. The phase purity of samples after the electrical conductivity measurement was checked by XRD of the crushed sample bars. Calculating the theoretical density based on XRD results of the sintered samples gives results in a difference of max. 4 % in density compared to using XRD results of the calcined powders.

# 3. Results

### 3.1 Crystal structure

X-ray diffraction patterns of the as-prepared spinel powders after calcination at 650 °C in air are shown in Figure 1. All materials are identified as single phase cubic spinels. The lattice parameters were determined by fitting the XRD patterns to the cubic *Fd-3m* space group with the cation distribution set to[1] $(Co^{2+})[Co^{3+}Mn^{3+}]O_4^{2-}$. Both iron (as $Fe^{3+}$) and copper (as $Cu^{2+}$) were added to the octahedral position in place of cobalt. There was no significant difference in the goodness of fit by placing Fe/Cu on the tetrahedral sites or with a different valence state. Lattice parameters obtained from the structure fit are plotted in Figure 2. Fe substitution increases the lattice parameter, while Cu substitution decreases the lattice parameter. This can also be seen in Figure 1 as a shifting of the diffraction peaks towards lower and higher 2θ angles, respectively. Neither of the substitutions result in a perfectly linear change in lattice parameter with compositions starting from the parent (MC) material.

XRD patterns of ceramics sintered at 1100 °C and annealed at 800 °C indicated that all materials remained single phase cubic spinels (Figure S3, Supplementary Material). The diffractograms were characterized by sharper peaks compared to Figure 1, reflecting the enhanced crystallinity and increase in particle size after heat treatment at higher temperature. The lattice parameters determined

[1] In accordance with conventions for describing the cation distribution in spinels, the round brackets () designate cations in tetrahedral sites, while the square brackets [] designate cations in octahedral sites.

by structure fitting of these patterns are plotted in Figure 2. For nearly all of the materials, the lattice parameter after sintering at 1100 °C + 800 °C is higher than for the as-prepared powder (calcined 650 °C). The largest difference is for the Cu-doped materials, which after sintering show increasing lattice parameter with increasing Cu substitution, i.e. the opposite trend of what is observed for the calcined powders. For the Fe-doped materials, the difference between the lattice parameters measured for the calcined powders and the sintered ceramics decreases with increasing Fe substitution. For the sintered samples the lattice parameter scales linearly with the site fraction of Fe, in accordance with Vegard's law, i.e.:

$$a_{MnCo_{2-x}Fe_xO_4} = a_{MnCo_2O_4} + 0.15x_{Fe} \quad (3)$$

where $a_{MnCo_{2-x}Fe_xO_4}$ is the lattice parameter of the Fe-doped material, $a_{MnCo_2O_4}$ is the lattice parameter of MnCo2O4 and $x_{Fe}$ is the site fraction of iron.

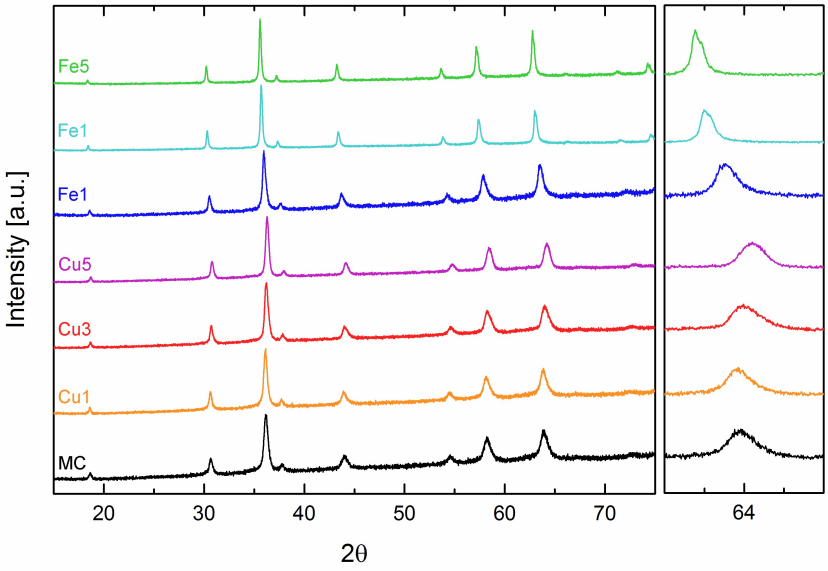


**Figure 1**. X-ray diffraction patterns of powders synthesized by spray pyrolysis after calcination at 650 °C in air. Individual patterns are normalized such that the highest intensity peak has the same intensity. The right-hand side of the figure shows an excerpt of the pattern between 63 and 65°.

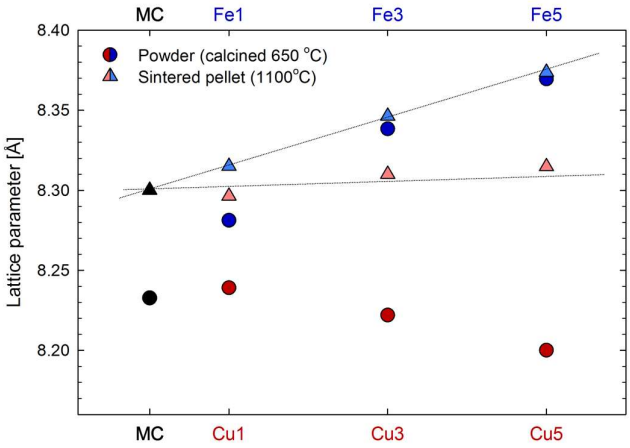


**Figure 2**. Lattice parameters determined by structure fitting of XRD patterns for as-prepared spinel powders(calcined at 650 °C), and pellets sintered at 1100 °C and annealed at 800 °C. MC is indicated

by black symbols, Fe-doped by blue and Cu-doped by red. Stippled lines are added as guide to the eye.

### 3.2 Thermal expansion coefficient

Thermal expansion measured by dilatometry during heating in air is shown in Figure 3a. The thermal expansion decreases nearly linearly with increasing substitution with Fe. Substitution with Cu results in an overall increase in thermal expansion, however, the variation with composition is more complicated and does not follow any obvious trend. For all materials, the expansion between room temperature and 800 °C can be well fitted with two linear segments, as illustrated in Figure 3b for $MnCo_2O_4$. The transition between the two segments varies with composition and is in the range of 300-500°C. The transition temperature for each material and the thermal expansion coefficients (TEC) calculated from the slopes of the curves in the different temperature intervals are summarized in Table 2. Measuring the same sample more than one time typically resulted in a difference of < 5 % in TEC (values reported in Table 2 are the first measurement of each sample).

There was a small negative hysteresis between the expansion measured during heating and cooling for all materials. For clarity, only the heating curves are shown in Figure 3 (full measurement in Figure S4, Supplementary material). The hysteresis decreases significantly when the measurement is performed between room temperature and 800 °C (Fig. S4 in the Supplementary Material), which indicates that the hysteresis is due to creep or possibly an onset of partial reduction of Co in the materials [39].

The material containing the highest fraction of copper, Cu5, displays a greater hysteresis compared to the other materials. A distinct change in the slope of thermal expansion above 800 °C can also be seen in Figure 3a. XRD of the crushed sample after testing, shown in Figure 4, reveals small amounts of CuO secondary phase. Thus, the change in slope for Cu5 is likely due to the transition from a single phase material ($MnCo_{1.5}Cu_{0.5}O_4$) to a dual phase mixture of $MnCo_{1.5+x}Cu_{0.5-x}O_4$ and CuO. The CuO secondary phase is not detected in the sintered pellet (also shown in Figure 4), possibly because it was under the detection limit of XRD (typically ~2 %) and/or this phase precipitated from the material with time at higher temperature.

**Table 2**: Thermal expansion coefficients (TEC) determined from linear fit of slopes in Figure 3a. Low temperature (LT) values are from 50 °C to the transition point, high temperature (HT) values are from the transition point to 800 °C. Sample density was determined by Archimedes method.

| Comp. | LT-TEC [$10^{-6}$ $K^{-1}$] | HT-TEC [$10^{-6}$ $K^{-1}$] | Transition point [°C] | TEC 50-800°C [$10^{-6}$ $K^{-1}$] | Sample density [%] |
|---|---|---|---|---|---|
| MC | 12.9 | 15.3 | 410 | 14.4 | 91 |
| Cu1 | 13.7 | 17.3 | 380 | 15.8 | 95 |
| Cu3 | 12.7 | 16.3 | 330 | 15.1 | 95 |
| Cu5 | 12.3 | 16.3 | 360 | 14.7 | 96 |
| Fe1 | 11.4 | 14.8 | 350 | 13.6 | 95 |
| Fe3 | 11.1 | 12.8 | 440 | 12.0 | 95 |
| Fe5 | 9.9 | 11.2 | 440 | 11.0 | 96 |

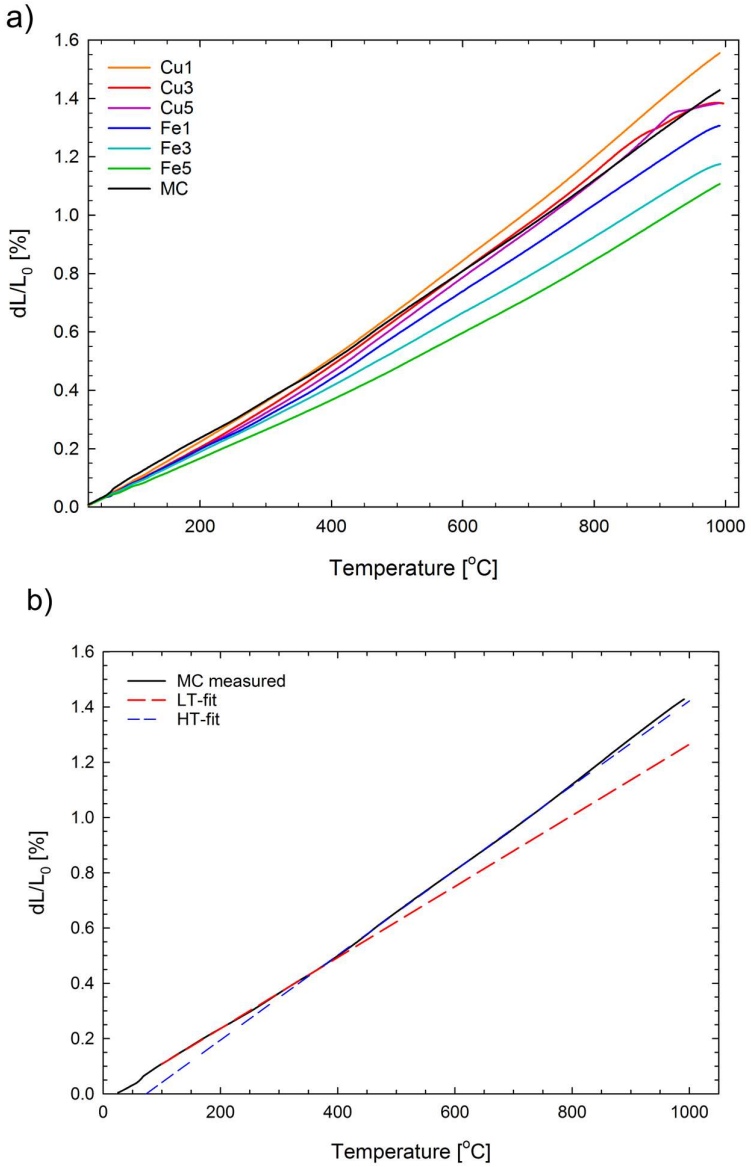


**Figure 3**. (a) Thermal expansion measured by dilatometry during heating in air, (b) Thermal expansion curve for the $MnCo_2O_4$ (MC) material showing linear fit of curve at low (LT) and high (HT) temperatures.

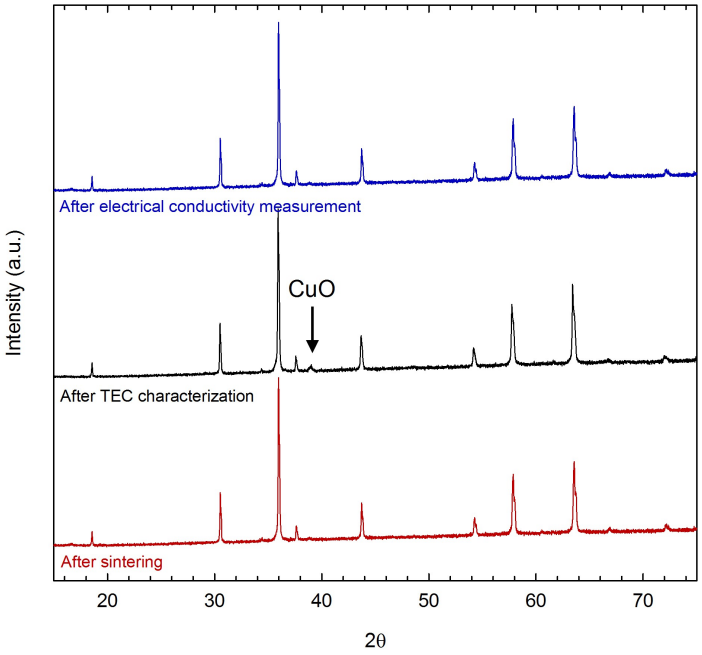


**Figure 4**. X-ray diffractograms of the $MnCo_{1.5}Cu_{0.5}O_4$ (Cu5) material after sintering (1100 °C + 800 °C, air), after thermal expansion characterization, and after electrical conductivity characterization. The peak belonging to CuO is highlighted, all other peaks belong to the cubic spinel phase.

### 3.3 Electrical conductivity

Figure 5 shows the electrical conductivity measured during cooling in air as a function of temperature. The conductivity value was recorded every 10 min and the 1 h long isotherms every 100 °C are visible from the higher density of points. The results have been corrected for sample porosity using equation (2). The conductivity increases nearly linearly with increasing site fraction of Cu and decreases nearly linearly with increasing site fraction of Fe. All materials exhibit semiconducting behavior. The temperature dependence can be described in accordance with the small polaron hopping model [68]:

$$\sigma = \frac{\sigma_0}{T} \exp\left(-\frac{E_A}{kT}\right) \quad (4)$$

where $T$ is the temperature [K], $E_A$ is the activation energy for hopping [eV], and $k$ is Boltzmann's constant [eV/K]. The pre-exponential factor, $\sigma_0$, is assumed to be constant. The slope of the ln(σT) vs 1/T curve (Fig. 5) can be fitted to two linear segments in similar temperature intervals as the thermal expansion curves, i.e. one segment between room temperature and ca. 400 °C and one at higher temperatures. The high temperature activation energy decreases nearly linearly from 0.53 eV to 0.41 eV with increasing site fraction of Cu, while Fe-substituted samples have the same activation energy as MC, namely 0.53 eV. The same trends are observed for the low temperature region, where Cu-substituted materials have activation energies in the range of 0.32-0.36 eV, while MC and the Fe-substituted materials have activation energies of 0.38-0.39 eV. The activation energy calculated from the slopes above 400 °C, the conductivity measured at 800 °C and the porosity of each sample are summarized in Table 3.

XRD of the crushed bars after measurement showed that all materials remained phase pure, cubic spinels. Unlike after TEC characterization, no CuO peaks could be detected in the diffractogram of the Cu5 material (see Figure 4). This is probably due to the different sintering procedures followed for

making samples for TEC (1100 °C + 800 °C) and for electrical conductivity (1050 °C). The lattice parameters of MC and Fe-substituted materials were equal to the lattice parameters obtained for the ceramics sintered at 1100 °C and annealed at 800 °C (see Figure 2). The lattice parameters for the Cu-substituted materials were in this case intermediate between those determined for calcined powder (650 °C) and sintered ceramic (1100 °C), decreasing from 8.286 Å for Cu1 to 8.274 Å for Cu5.

**Table 3**: Electrical conductivity ($\sigma$) measured at 800 °C, activation energy ($E_A$) and pre-exponential factor ($\sigma_0$) at high temperature (>400 °C) extracted from the Arrhenius plots. The conductivity values have been corrected for the measured sample density. $\sigma_{uncorr}$ is the electrical conductivity at 800 °C before correcting for porosity.

| Comp. | $E_A$ [eV] | $\sigma_0$ | $\sigma$ (800 °C) [S/cm] | Sample density [%] | $\sigma_{uncorr}$ [S/cm] |
|---|---|---|---|---|---|
| MC | 0.53 | 17.2 | 89 | 72 | 55 |
| Cu1 | 0.50 | 17.1 | 114 | 84 | 87 |
| Cu3 | 0.44 | 16.7 | 142 | 95 | 131 |
| Cu5 | 0.41 | 16.5 | 168 | 96 | 155 |
| Fe1 | 0.53 | 17.1 | 77 | 77 | 52 |
| Fe3 | 0.53 | 16.5 | 47 | 79 | 33 |
| Fe5 | 0.53 | 16.2 | 31 | 81 | 23 |

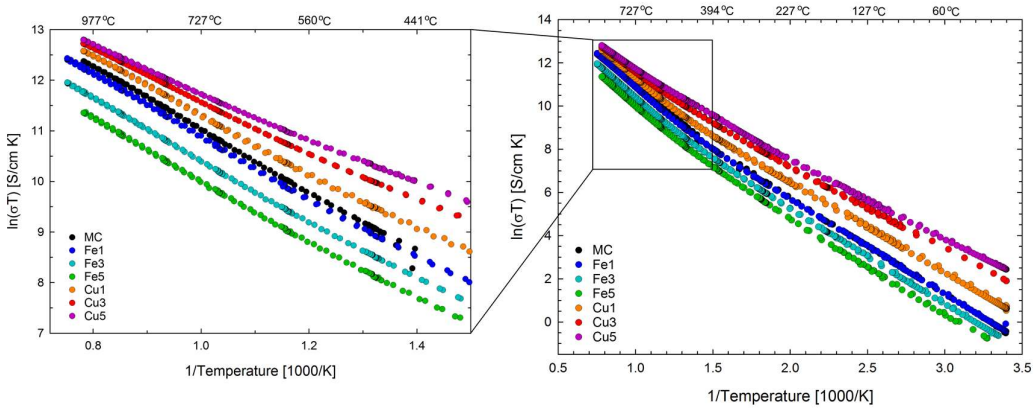


**Figure 5**. Arrhenius plot of the electrical conductivity as a function of temperature, measured during cooling. Results are corrected for sample porosity (specified in Table 3).

In most cases, there was a negligible (< 1 %) hysteresis between the conductivity measured during heating and cooling. However, for the MC sample, the conductivity measured during the 1 h isotherm at 375 °C decreased considerably with time. When this sample was heated up to 1000 °C and cooled, the conductivity measured below 500 °C during cooling was higher than measured during heating, as seen in Figure 6a. Figure 6b shows that the electrical conductivity of the MC sample decreases more than 180 % over 40-50 h at constant temperature of 325 °C or 275 °C. The initial conductivity at both temperatures was re-established by heating the sample above 500 °C. In contrast, the electrical conductivity measured at 800 °C changes by less than 0.4 % over 25 h (Fig. 6b insert). A sample of the Cu1 material with 60 % density (sintered 10 h at 950 °C in air) also showed a hysteresis between the heating and cooling segments (Figure S5, Supplementary Material). This was not observed for the same material when the sample density was 84 % (sintered 5 h at 1050 °C in air), which suggests that the relaxation in electrical conductivity at low temperature is related to the sample's interaction with the atmosphere.

Based on several measurements on three different MC samples having similar density (70-73 %), the error in the electrical conductivity measurement is estimated to be ~ 1 %. The error when

correcting for the sample porosity is significantly larger. For the two Cu1 samples having a density of 60 and 84 % (Figure S5, Supplementary Material), the electrical conductivity at 800 °C differed by ~ 20 % after correcting for porosity. Accordingly, we consider the conductivity reported for the denser samples to be more reliable.

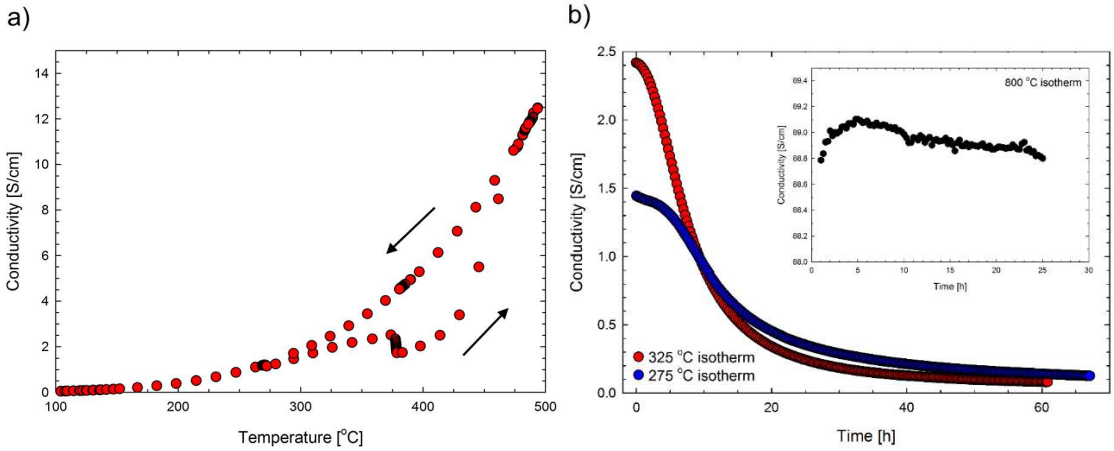


**Figure 6**. Electrical conductivity of $MnCo_2O_4$ (72 % density). The conductivity is corrected for sample porosity. (a) Hysteresis in electrical conductivity measured during heating and cooling. The plot is an excerpt from a measurement between room temperature and 1000 °C. (b) Conductivity as a function of time, measured at constant temperature

### 3.4 Thermogravimetric analysis

To investigate possible origins of the hysteresis in electrical conductivity, MC powder obtained from a crushed ceramic sintered at 1100 °C and annealed at 800 °C was analyzed by thermogravimetry. Figure 7 shows that the sample mass increases upon heating above ca. 200 °C, reaching a maximum at 370 °C before it decreases again. Between 510 and 800 °C the mass is nearly constant. Upon cooling, the same trends are observed, but the mass gain is shifted to a lower temperature. The mass gain around 400 °C is reproduced when the same sample is re-heated after cooling (Figure S6 in the Supplementary Material). TGA of the as-prepared (calcined 650 °C) powders of MC, Fe3 and Cu3 resulted in similar observations (Figure S7 in the Supplementary Material). Notably, for all of materials there is a peak in the mass change curve between 350 and 400 °C. Overall, the mass changes are considerably larger for the powder calcined at 650 °C than for the powder obtained from a crushed ceramic sintered at 1100 °C. The calcined powders experienced a continuous mass loss from the peak at 350-400 °C to 800 °C.

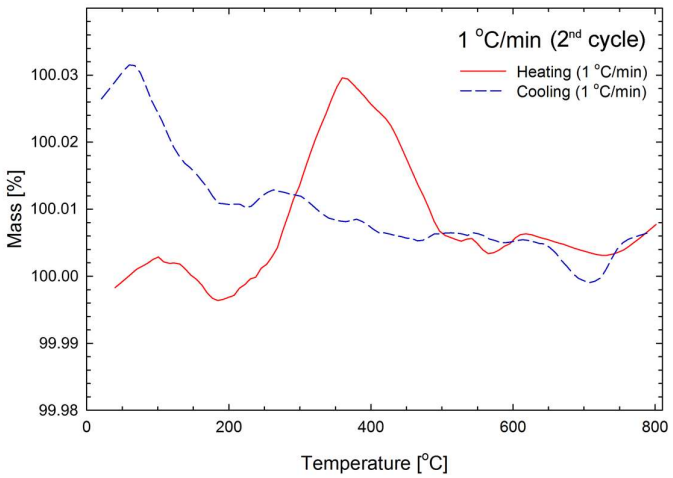


**Figure 7.** Thermogravimetric analysis of $MnCo_2O_4$ powder (obtained from a crushed ceramic sintered 1100 °C+ 800 °C) showing relative weight change as a function of temperature in air.

# 4. Discussion

## 4.1 Crystal structure

A smaller lattice parameter is measured for most of the materials after calcination at 650 °C compared to after sintering at 1100 °C (Fig. 2). This is consistent with the temperature dependence of the lattice parameter for $MnCo_2O_4$ reported in literature [32,44,69]. $MnCo_2O_4$ prepared below ca. 500-600°C is reported to be cation deficient, with a smaller lattice parameter compared to the stoichiometric material [34,40–44]. Comparing the value for the MC powder calcined at 650 °C (8.233 Å) with the value given in PDF 23-1237 for presumably stoichiometric $MnCo_2O_4$ prepared at 720 °C (8.269 Å) indicates that the as-prepared powder is slightly cation deficient. Nissinen et al. [40] reported $\delta = 0.1$ for $MnCo_2O_{4+\delta}$ calcined at 640 °C. With increasing Fe-substitution the difference between the lattice parameters after the 650 °C and 1100 °C heat treatments decreases, indicating that the as prepared Fe-doped powder has a lower cation deficiency.

Due to the similar scattering factors of the elements in $MnCo_2O_4$, the cation distribution cannot be determined from XRD data. However, the most probable cation distribution may be estimated by comparing the lattice parameter determined by XRD with the theoretical lattice parameter for different cation distributions, following the method of O'Neill and Navrotsky [70]. The method is based on geometrical considerations of the spinel structure, described by Hill et al. [71], and assumes that the ions can be considered as hard spheres. The average ionic radius is used when multiple cations occupy the same site. Based on an extensive review of binary spinels, O'Neill and Navrotsky [70] derived a set of effective ionic radii for cations in the spinel structure, which are used in the calculation. These radii are in most cases slightly smaller than Shannon radii, which are derived as an average over a large number of different structures [72]. The theoretical lattice parameter, a, is obtained from:

$$a = R_{oct}(3u^2 - 2u + 3/8)^{1/2} \quad (5)$$

where $R_{oct}$ is the octahedral cation-anion bond length and u is the oxygen anion parameter, given by:

$$u = \frac{R^2/4 - 2/3 + (11R^2/48 - 1/18)^{1/2}}{2R^2 - 2} \quad (6)$$

where R is the ratio of the octahedral to tetrahedral cation-anion bond length.

In the following, the calculated lattice parameters are compared to the lattice parameters determined for sintered samples (1100 °C + 800 °C), since the electrical conductivity and thermal expansion was measured on these samples.

For MC, $Co^{2+}$ is assumed to be the only cation occupying tetrahedral sites, in accordance with the majority of the cation distributions previously suggested in literature [32–39]. The cation distribution resulting in the closest match with the lattice parameter determined by XRD (8.298 Å) is $(Co^{2+})[Mn^{3+}_{0.54}Mn^{4+}_{0.46}Co^{3+}_{0.54}Co^{2+}_{0.46}]O_4^{2-}$, which has a theoretical lattice parameter of 8.298 Å. This distribution is nearly identical to that suggested by Bordeneuve et al. [39] based on neutron diffraction data on a sample sintered at 750 °C and quenched to room temperature. The nearly 1:1 $Mn^{3+}$:$Mn^{4+}$ ratio accounts for the high electrical conductivity of $MnCo_2O_4$ in the series of $Mn_xCo_{3-x}O_4$ spinels [47].

Addition of a third cation (Cu/Fe) complicates the calculation. However, taking the above suggested distribution for MC as the starting point, two possibilities with an almost equally good match between calculated and measured lattice parameters are obtained for the Fe-substituted materials. The first possibility is that $Fe^{3+}$ (0.645 Å) replaces $Co^{3+}$ (0.53 Å) on the octahedral sites, and the second is that $Fe^{3+}$ (0.485 Å) replaces $Co^{2+}$ (0.58 Å) on tetrahedral sites. The latter requires a charge compensation by reduction of Co and Mn on the octahedral sites, resulting in the distribution $(Fe^{3+}_{0.5}Co^{2+}_{0.5})[Mn^{3+}_{0.5}Mn^{4+}_{0.5}Co^{2+}]O_4^{2-}$ for Fe5. In both options for the cation distribution, the increasing site fraction of Fe reduces the site fraction of $Co^{3+}$ on octahedral sites. This makes both cation distributions consistent with the electrical conductivity and thermal expansion results, as will be discussed in Sections 4.2 and 4.3.

Previous investigations of the cation distribution in $MnCo_{2-x}Fe_xO_4$ have suggested both a mixed occupancy of Fe on tetrahedral and octahedral sites [48], and that Fe mainly occupies the latter [73]. Crystal field theory predicts that both $Mn^{3+}$ and $Co^{3+}$ have a stronger preference for the octahedral site than $Fe^{3+}$ [74]. It is therefore more likely that $Fe^{3+}$ replaces $Co^{2+}$ on tetrahedral sites in $MnCo_{2-x}Fe_xO_4$ and that the increase in lattice parameter is due to charge compensation by Co (and Mn) on the octahedral sites.

The lattice parameters of the Cu-substituted materials varied greatly with thermal history. The number of possibilities in terms of site occupancy and oxidation state of the elements are too numerous to use the method developed by O'Neill and Navrotsky to explain this variation. Investigations of $MnCoCuO_4$ have resulted in conflicting suggestions for the cation distribution. Brabers and Setten [75] suggested the distribution $(Cu^{+}_{0.65}Mn^{3+}_{0.35})[Cu^{2+}_{0.35}Co^{3+}Mn^{4+}_{0.65}]O^{2-}_4$, while others have suggested that both $Cu^{2+}$ and $Cu^{+}$ occupy tetrahedral sites and that octahedral sites are occupied by $Co^{3+}$ and $Mn^{3+/4+}$ [76,77]. The different cation distributions are likely due to differences in thermal history of the samples. As discussed in Section 4.2, the electrical conductivity results suggest a mixed occupancy of $Cu^{+}$ and $Cu^{2+}$ on the octahedral sites.

### 4.2 Electrical conductivity

The electrical conductivity of $MnCo_2O_4$ determined in this work is in the upper range of the values previously reported in literature. For example, [49] reported 34 S/cm at 800 °C in air for a sample sintered at 1200 °C and [78] reported 40 S/cm for a sample sintered at 1300 °C. As previously discussed by Liu et al. [48] some of the discrepancies found in literature are most likely due to the high temperature at which many of the investigated samples have been sintered. According to the $Mn_3O_4$-$Co_3O_4$ phase diagram reported by Aukrust and Muan [65], the $MnCo_2O_4$ spinel is only stable up to ca. 1050 °C in air. Liu et al. [48] showed that $MnCo_2O_4$ sintered at 1200 °C had an electrical conductivity of 51 S/cm at 800 °C and contained significant amounts of rock salt secondary phases. When the same sample was annealed at 1000 °C for 72 h, the rock salt phases disappeared and the electrical conductivity at 800 °C increased to 87 S/cm. This is close to the value we obtained (89 S/cm) for the same material sintered at 1050 °C, which was confirmed to be phase pure by XRD.

The electrical conductivity decreases nearly linearly with increasing site fraction of Fe, without any changes in the activation energy. If hopping between $Co^{3+}$-$Co^{2+}$ pairs on the octahedral sites

contributes to the charge transfer in $MnCo_2O_4$, as suggested by Rousset et al. [47], both of the above suggested cation distributions for the Fe-substituted materials would explain why the electrical conductivity decreases and there is no change in the activation energy. Irrespective of whether $Fe^{3+}$ resides on the octahedral or tetrahedral sites in the spinel structure, the consequence of introducing Fe is a decrease in the concentration of $Co^{3+}$ (see section 4.1). Thus, there are fewer available sites for hopping as charge transfer is limited to hopping between the $Mn^{3+}$-$Mn^{4+}$ pairs.

With increasing Cu-substitution the electrical conductivity increases and the activation energy decreases. The change in activation energy indicates that copper ions participate directly in the charge transfer. Since small polaron hopping in the spinel structure is feasible only between equivalent sites, and the cation-cation distance is shortest between the octahedral sites, this implies that both $Cu^{+}$ and $Cu^{2+}$ occupy the octahedral sites.

The decrease in electrical conductivity over time, as seen around 375 °C in Figure 6, has previously been reported for nickel and copper ferrite spinels and attributed to re-distribution of the cations between octahedral and tetrahedral sites [79,80]. Rousset el at. [47] investigated this so-called "aging" phenomenon in the $Mn_xCo_{3-x}O_4$-system at 125 °C and also attributed a decreasing electrical conductivity with time to cation re-distribution. However, aging was only appreciable for the end members of the system ($2.8<x<1.5$); for $MnCo_2O_4$ the change in electrical conductivity was less than 0.1 % over 500 h at 125 °C. Here, we measured a considerable aging effect also for the $MnCo_2O_4$ composition. Since the effect only was observed for this particular sample (with 72 % density) and a Cu1 sample sintered to low density (60%), the effect is most likely connected to interactions with the atmosphere. The $MnCo_2O_4$ sample investigated by Rousset et al. was prepared by spark plasma sintering, resulting in a density of 95 %, which is significantly higher than the density of the $MnCo_2O_4$ sample measured here (72 %) [47].

The mass changes observed by TGA during heating (Figure 7) provide a basis to explain the time variation of the electrical conductivity. The sample mass increase between 200-370 °C is likely due to oxidation and formation of cation vacancies, which may be described in terms of Kroger-Vink notation as [81]:

$$\frac{1}{2}O_2 \rightarrow O_O^X + \frac{1}{4}V_A'' + \frac{1}{2}V_B''' + 2p^* \qquad (7)$$

where $O_O^X$ represents an oxide ion on a regular oxide ion site, $V_A''$ represents an A-site vacancy with double negative charge, $V_B'''$ represents a B-site vacancy with triple negative charge, and $p^*$ represents an a hole with a positive charge. That is, oxidation results in the formation of a new unit cell by creation of cation vacancies on the tetrahedral (A) and octahedral (B) sites, and results in two electron holes. $MnCo_2O_4$ is a p-type conductor [82], so intuitively, it may be expected that the increase in hole concentration should result in an increase in electrical conductivity [45]. However, as discussed by Groen et al. [81], in this case the mobility of the charge carriers is more important than their concentration. The creation of cation vacancies reduces the number of available sites for hopping and consequently the mobility. When heated above 400 °C, oxygen is removed and cationic vacancies are annihilated, which results in an increase in the electrical conductivity.

Using X-ray absorption near edge structure (XANES) analysis, Bazuev et al. [69] demonstrated that the $Mn^{4+}/Mn^{3+}$ fraction in $MnCo_2O_{4+\delta}$ spinel increases with increasing $\delta$. Accordingly, it may be inferred that the electron holes are localized on manganese cations, i.e. $Mn^{3+} \rightarrow Mn^{4+}$ during oxidation. Above 370 °C the mass loss likely corresponds to reduction of $Mn^{4+}$ to $Mn^{3+}$, as suggested previously for heating of cation-deficient $MnCo_2O_{4+\delta}$ [69]. For the calcined powders (650 °C), the mass loss continued to decrease upon heating to 800 °C. This is probably due to reduction of $Co^{III}$ to $Co^{2+}$ on the octahedral sites, considering that $Co_3O_4$ has the lowest decomposition temperature (900 °C) in the $Mn_xCo_{3-x}O_4$ series of spinels [39].

### 4.3 Thermal expansion

All materials exhibited a change in the slope of thermal expansion above ca. 400 °C. Similar behavior may be observed upon examination of several previously published thermal expansion curves for

$MnCo_2O_4$ and $MnCo_{2-x}Cu_xO_4$, although this was not explicitly discussed by the authors [49,50,83,84]. $MnCo_2O_4$ has no recognized phase transitions in the temperature interval where the TEC is observed to increase. Some calculated phase diagrams of the Mn-Co-O system suggest the coexistence of $CoMnO_3$ with $MnCo_2O_4$ below ca. 600 °C and precipitation of $MnO_2$ below ca. 400 °C [53] . However, as far as we are aware, this has never been observed experimentally. A magnetic transition can be excluded as the Curie temperature of $MnCo_2O_4$ is 180 K [63].

The most likely mechanism behind the increase in the TEC is a spin state transition of cobalt on the octahedral sites, which is responsible for the extra thermal expansion of $Co_3O_4$ observed above ca. 350 °C [85]. This can be described as $Co^{3+}$(LS) (0.545 Å) → $Co^{3+}$(HS) (0.61Å), where the numbers in parentheses are the Shannon ionic radii. Three-valent cobalt residing in the octahedral sites of $MnCo_2O_4$ is believed to be in the low spin state at room temperature [39], so a transition to high spin with increasing temperature is feasible. A mechanism involving spin state transition of cobalt would explain why the thermal expansion becomes more linear over the whole investigated temperature range when cobalt is replaced by iron. As discussed above, both of the most probable cation distributions for Fe-substituted $MnCo_2O_4$ involve a lower concentration of $Co^{3+}$ on octahedral sites. Mössbauer spectroscopy or a similar technique is required to confirm or falsify whether the observed TEC change can be related to a spin state transition, for now it must be considered a postulate.

The thermal expansion behavior of materials containing copper is more complicated and the TEC does not follow any obvious trend with composition. Furthermore, the lattice parameter varies significantly with the thermal history of the sample. This is most likely due to precipitation of CuO as a secondary phase, which indeed was observed for the sample containing the highest amount of Cu, namely $MnCo_{1.5}Cu_{0.5}O_4$. Precipitation of CuO may also have taken place in samples with a lower Cu substitution, but in a quantity below the detection limit of XRD.

### 4.4 Suitability as SOFC interconnect coating materials

As mentioned in the introduction, the most important criteria for selection of a suitable coating material for the protection of SOFC metallic interconnects are a close TEC match to the alloy and other SOFC components, a sufficiently high electrical conductivity and low oxygen and chromium diffusion coefficients through the coating. With respect to thermal expansion, the Fe-substituted materials show greatest promise. The average TEC of $MnCo_{1.7}Fe_{0.3}O_4$ (Fe3) between 50-800°C ($12.0\times10^{-6}$ $K^{-1}$) is very close to the TEC of Crofer 22 APU ($11.9\times10^{-6}$ $K^{-1}$ [14]) in the same temperature interval, which is one of the commonly used interconnect alloys today. A closer match in TEC leads to less build-up of stresses during thermal cycling, thereby reducing the risk of cracking and/or spallation of the coating. Although the electrical conductivity was reduced by doping with iron, the conductivity remains several orders of magnitude higher than the typical electrical conductivity of the oxide scale formed on FSS [4]. The area specific resistance (ASR) for a coated interconnect will scale with the thickness and resistivity of each layer. Assuming the scale is made of $Cr_2O_3$ with an electrical conductivity of 0.1 S/cm at 800 °C, and that the coating is a 20 μm thick layer of Fe5 (31 S/cm at 800 °C), the $Cr_2O_3$ scale will dominate the ASR once this scale grows thicker than 0.03 μm. This suggests that in order to lower the ASR reducing the oxidation rate of the alloy is more important than increasing the conductivity of the coating material. We have previously shown that the MC, Fe3 and Cu3 materials result in nearly the same ASR after more than 4000 h oxidation at 800 °C when applied as a coating on Crofer 22 APU [28,30].

## 5. Conclusion

Single phase $MnCo_{2-x}M_xO_4$ (M=Cu, Fe; x = 0.1, 0.3, 0.5) materials of the cubic spinel structure were synthesized by spray pyrolysis. The thermal expansion behavior of all materials is characterized by a lower TEC between room temperature and ca. 400 °C compared to between ca. 400 °C and 800 °C. It is suggested that a spin state transition of $Co^{3+}$ from low spin to high spin is the most likely origin of the increased expansion at elevated temperatures. Substitution with Fe results in a more linear

expansion behavior in the whole temperature interval and an overall lower TEC. The thermal expansion behavior of Cu-substituted materials is likely influenced by precipitation of CuO secondary phases and the TEC values are generally slightly higher than that of $MnCo_2O_4$.

The electrical conductivity of $MnCo_2O_4$ (89 S/cm at 800 °C) decreases with increasing site fraction of Fe, reaching 31 S/cm for Fe5, and increases with increasing site fraction of Cu, reaching 168 S/cm for Cu5. The changes in electrical conductivity are almost in direct proportion with the number of sites available for polaron hopping and can thus easily be rationalized.

Based on the closest match in TEC to other SOFC materials, Fe doped $MnCo_2O_4$ is considered most promising for the application as a protective coating on SOFC metallic interconnects.

**Funding**
Financial support from the Faculty of Natural Sciences at NTNU is acknowledged.

## References

[1] J.R. Mawdsley, J. David Carter, A. Jeremy Kropf, B. Yildiz, V.A. Maroni, Post-test evaluation of oxygen electrodes from solid oxide electrolysis stacks, Int. J. Hydrog. Energy. 34 (2009) 4198–4207. doi:10.1016/j.ijhydene.2008.07.061.

[2] N.H. Menzler, D. Sebold, Q. Fang, Chromium-Related Degradation of Thin-Film Electrolyte Solid Oxide Fuel Cell Stacks, ECS Trans. 68 (2015) 1815–1825. doi:10.1149/06801.1815ecst.

[3] M. Palcut, L. Mikkelsen, K. Neufeld, M. Chen, R. Knibbe, P.V. Hendriksen, Corrosion stability of ferritic stainless steels for solid oxide electrolyser cell interconnects, Corros. Sci. 52 (2010) 3309–3320. doi:10.1016/j.corsci.2010.06.006.

[4] A. Holt, P. Kofstad, Electrical conductivity and defect structure of $Cr_2O_3$. II. Reduced temperatures (< 1000 °C), Solid State Ion. 69 (1994) 137–143.

[5] Z. Lu, J. Zhu, E. Andrew Payzant, M.P. Paranthaman, Electrical Conductivity of the Manganese Chromite Spinel Solid Solution, J. Am. Ceram. Soc. 88 (2005) 1050–1053. doi:10.1111/j.1551-2916.2005.00205.x.

[6] W.Z. Zhu, S.C. Deevi, Opportunity of metallic interconnects for solid oxide fuel cells: a status on contact resistance, Mater. Res. Bull. 38 (2003) 957–972. doi:10.1016/S0025-5408(03)00076-X.

[7] K. Hilpert, D. Das, M. Miller, D.H. Peck, R. Weiß, Chromium Vapor Species over Solid Oxide Fuel Cell Interconnect Materials and Their Potential for Degradation Processes, J. Electrochem. Soc. 143 (1996) 3642–3647. doi:10.1149/1.1837264.

[8] E.J. Opila, D.L. Myers, N.S. Jacobson, I.M.B. Nielsen, D.F. Johnson, J.K. Olminsky, M.D. Allendorf, Theoretical and Experimental Investigation of the Thermochemistry of $CrO_2(OH)_2(g)$, J. Phys. Chem. A. 111 (2007) 1971–1980. doi:10.1021/jp0647380.

[9] H. Yokokawa, T. Horita, N. Sakai, K. Yamaji, M.E. Brito, Y.-P. Xiong, H. Kishimoto, Thermodynamic considerations on Cr poisoning in SOFC cathodes, Solid State Ion. 177 (2006) 3193–3198. doi:10.1016/j.ssi.2006.07.055.

[10] J.J. Bentzen, J.V.T. Høgh, R. Barfod, A. Hagen, Chromium Poisoning of LSM/YSZ and LSCF/CGO Composite Cathodes, Fuel Cells. 9 (2009) 823–832. doi:10.1002/fuce.200800143.

[11] J.W. Fergus, Effect of cathode and electrolyte transport properties on chromium poisoning in solid oxide fuel cells, Int. J. Hydrog. Energy. 32 (2007) 3664–3671. doi:10.1016/j.ijhydene.2006.08.005.

[12] N. Shaigan, W. Qu, D.G. Ivey, W. Chen, A review of recent progress in coatings, surface modifications and alloy developments for solid oxide fuel cell ferritic stainless steel interconnects, J. Power Sources. 195 (2010) 1529–1542. doi:10.1016/j.jpowsour.2009.09.069.

[13] A. Nakajo, J. Kuebler, A. Faes, U.F. Vogt, H.J. Schindler, L.-K. Chiang, S. Modena, J. Van herle, T. Hocker, Compilation of mechanical properties for the structural analysis of solid oxide fuel cell stacks. Constitutive materials of anode-supported cells, Ceram. Int. 38 (2012) 3907–3927. doi:10.1016/j.ceramint.2012.01.043.

[14] Thyssen Krupp, Crofer 22 APU Material Data Sheet No. 4046, (2010).

[15] K. Huang, P.Y. Hou, J.B. Goodenough, Reduced area specific resistance for iron-based metallic interconnects by surface oxide coatings, Mater. Res. Bull. 36 (2001) 81–95. doi:10.1016/S0025-5408(01)00506-2.
[16] S. Fontana, S. Chevalier, G. Caboche, Metallic interconnects for solid oxide fuel cell: Performance of reactive element oxide coating during long time exposure, Mater. Corros. 62 (2011) 650–658. doi:10.1002/maco.201005857.
[17] Å.H. Persson, L. Mikkelsen, P.V. Hendriksen, M.A.J. Somers, Interaction mechanisms between slurry coatings and solid oxide fuel cell interconnect alloys during high temperature oxidation, J. Alloys Compd. 521 (2012) 16–29. doi:10.1016/j.jallcom.2011.12.095.
[18] M. Palcut, L. Mikkelsen, K. Neufeld, M. Chen, R. Knibbe, P.V. Hendriksen, Improved oxidation resistance of ferritic steels with LSM coating for high temperature electrochemical applications, Int. J. Hydrog. Energy. 37 (2012) 8087–8094. doi:10.1016/j.ijhydene.2011.11.138.
[19] S. Molin, M. Chen, P.V. Hendriksen, Oxidation study of coated Crofer 22 APU steel in dry oxygen, J. Power Sources. 251 (2014) 488–495. doi:10.1016/j.jpowsour.2013.09.100.
[20] Y. Larring, T. Norby, Spinel and Perovskite Functional Layers Between Plansee Metallic Interconnect (Cr-5 wt % Fe-1 wt % $Y_2O_3$) and Ceramic $(La_{0.85}Sr_{0.15})_{0.91}MnO_3$ Cathode Materials for Solid Oxide Fuel Cells, J. Electrochem. Soc. 147 (2000) 3251–3256. doi:10.1149/1.1393891.
[21] B. Hua, J. Pu, W. Gong, J. Zhang, F. Lu, L. Jian, Cyclic oxidation of Mn–Co spinel coated SUS 430 alloy in the cathodic atmosphere of solid oxide fuel cells, J. Power Sources. 185 (2008) 419–422. doi:10.1016/j.jpowsour.2008.06.055.
[22] T. Uehara, N. Yasuda, M. Okamoto, Y. Baba, Effect of Mn–Co spinel coating for Fe–Cr ferritic alloys ZMG232L and 232J3 for solid oxide fuel cell interconnects on oxidation behavior and Cr-evaporation, J. Power Sources. 196 (2011) 7251–7256. doi:10.1016/j.jpowsour.2010.11.078.
[23] J.W. Stevenson, Z.G. Yang, G.G. Xia, Z. Nie, J.D. Templeton, Long-term oxidation behavior of spinel-coated ferritic stainless steel for solid oxide fuel cell interconnect applications, J. Power Sources. 231 (2013) 256–263. doi:10.1016/j.jpowsour.2013.01.033.
[24] S.-I. Lee, J. Hong, H. Kim, J.-W. Son, J.-H. Lee, B.-K. Kim, H.-W. Lee, K.J. Yoon, Highly Dense Mn-Co Spinel Coating for Protection of Metallic Interconnect of Solid Oxide Fuel Cells, J. Electrochem. Soc. 161 (2014) F1389–F1394. doi:10.1149/2.0541414jes.
[25] Z. Yang, G. Xia, S.P. Simner, J.W. Stevenson, Thermal Growth and Performance of Manganese Cobaltite Spinel Protection Layers on Ferritic Stainless Steel SOFC Interconnects, J. Electrochem. Soc. 152 (2005) A1896–A1901. doi:10.1149/1.1990462.
[26] N.V. Gavrilov, V.V. Ivanov, A.S. Kamenetskikh, A.V. Nikonov, Investigations of Mn–Co–O and Mn–Co–Y–O coatings deposited by the magnetron sputtering on ferritic stainless steels, Surf. Coat. Technol. 206 (2011) 1252–1258. doi:10.1016/j.surfcoat.2011.08.036.
[27] H.H. Zhang, C.L. Zeng, Preparation and performances of Co–Mn spinel coating on a ferritic stainless steel interconnect material for solid oxide fuel cell application, J. Power Sources. 252 (2014) 122–129. doi:10.1016/j.jpowsour.2013.12.007.
[28] S. Molin, P. Jasinski, L. Mikkelsen, W. Zhang, M. Chen, P.V. Hendriksen, Low temperature processed $MnCo_2O_4$ and $MnCo_{1.8}Fe_{0.2}O_4$ as effective protective coatings for solid oxide fuel cell interconnects at 750 °C, J. Power Sources. 336 (2016) 408–418. doi:10.1016/j.jpowsour.2016.11.011.
[29] H. Kurokawa, C.P. Jacobson, L.C. DeJonghe, S.J. Visco, Chromium vaporization of bare and of coated iron–chromium alloys at 1073 K, Solid State Ion. 178 (2007) 287–296. doi:10.1016/j.ssi.2006.12.010.
[30] B. Talic, S. Molin, K. Wiik, P.V. Hendriksen, H.L. Lein, Comparison of iron and copper doped manganese cobalt spinel oxides as protective coatings for solid oxide fuel cell interconnects, J. Power Sources. 372 (2017) 145–156. doi:10.1016/j.jpowsour.2017.10.060.
[31] B. Talic, H. Falk-Windisch, V. Venkatachalam, P.V. Hendriksen, K. Wiik, H.L. Lein, Effect of coating density on oxidation resistance and Cr vaporization from solid oxide fuel cell interconnects, J. Power Sources. 354 (2017) 57–67. doi:10.1016/j.jpowsour.2017.04.023.
[32] N. Yamamoto, S. Higashi, S. Kawano, N. Achiwa, Preparation of $MnCo_2O_4$ by a wet method and its metal ion distribution, J. Mater. Sci. Lett. 2 (1983) 525–526. doi:10.1007/BF00721473.

[33] S. Naka, M. Inagaki, T. Tanaka, On the formation of solid solution in $Co_{3-x}Mn_xO_4$ system, J. Mater. Sci. 7 (1972) 441–444. doi:10.1007/BF00553768.
[34] E. Rios, J.-L. Gautier, G. Poillerat, P. Chartier, Mixed valency spinel oxides of transition metals and electrocatalysis: case of the $Mn_xCo_{3-x}O_4$ system, Electrochimica Acta. 44 (1998) 1491–1497. doi:10.1016/S0013-4686(98)00272-2.
[35] A. Purwanto, A. Fajar, H. Mugirahardjo, J.W. Fergus, K. Wang, Cation distribution in spinel $(Mn,Co,Cr)_3O_4$ at room temperature, J. Appl. Crystallogr. 43 (2010) 394–400. doi:10.1107/S0021889810008150.
[36] H. Bordeneuve, C. Tenailleau, S. Guillemet-Fritsch, R. Smith, E. Suard, A. Rousset, Structural variations and cation distributions in $Mn_{3-x}Co_xO_4$ ($0 \le x \le 3$) dense ceramics using neutron diffraction data, Solid State Sci. 12 (2010) 379–386. doi:10.1016/j.solidstatesciences.2009.11.018.
[37] B. Boucher, R. Buhl, R. Di Bella, M. Perrin, Etude par des mesures de diffraction de neutrons et de magnétisme des propriétés cristallines et magnétiques de composés cubiques spinelles $Co_{3-x}Mn_xO_4$($0,6 \le x \le 1,2$), J. Phys. 31 (1970) 113–119. doi:10.1051/jphys:01970003101011300.
[38] D.G. Wickham, W.J. Croft, Crystallographic and magnetic properties of several spinels containing trivalent JA-1044 manganese, J. Phys. Chem. Solids. 7 (1958) 351–360. doi:10.1016/0022-3697(58)90285-3.
[39] H. Bordeneuve, A. Rousset, C. Tenailleau, S. Guillemet-Fritsch, Cation distribution in manganese cobaltite spinels $Co_{3-x}Mn_xO_4$ ($0 \le x \le 1$) determined by thermal analysis, J. Therm. Anal. Calorim. 101 (2010) 137–142. doi:10.1007/s10973-009-0557-7.
[40] T. Nissinen, M. Leskelä, M. Gasik, J. Lamminen, Decomposition of mixed Mn and Co nitrates supported on carbon, Thermochim. Acta. 427 (2005) 155–161. doi:10.1016/j.tca.2004.09.005.
[41] K. Uusi-Esko, E.-L. Rautama, M. Laitinen, T. Sajavaara, M. Karppinen, Control of Oxygen Nonstoichiometry and Magnetic Property of $MnCo_2O_4$ Thin Films Grown by Atomic Layer Deposition, Chem. Mater. 22 (2010) 6297–6300. doi:10.1021/cm102003y.
[42] J.L. Gautier, C. Cabezas, S. Barrato, Reduction electrochimique de $MnCo_2O_4$ prepare a basse et haute temperature, Electrochimica Acta. 26 (1981) 1377–1382. doi:10.1016/0013-4686(81)90005-0.
[43] O.I. Gyrdasova, G.V. Bazuev, I.G. Grigorov, O.V. Koryakova, Preparation of $MnCo_2O_4$ whiskers and spheroids through thermal decomposition of $Mn_{1/3}Co_{2/3}C_2O_4 \cdot 2H_2O$, Inorg. Mater. 42 (2006) 1126–1132. doi:10.1134/S0020168506100141.
[44] A. Restovic, E. Ríos, S. Barbato, J. Ortiz, J.L. Gautier, Oxygen reduction in alkaline medium at thin $Mn_xCo_{3-x}O_4$ ($0 \le x \le 1$) spinel films prepared by spray pyrolysis. Effect of oxide cation composition on the reaction kinetics, J. Electroanal. Chem. 522 (2002) 141–151. doi:10.1016/S0022-0728(02)00639-3.
[45] C.N.R. Rao, G.V. Subba Rao, Electrical conduction in metal oxides, Phys. Status Solidi A. 1 (1970) 597–652. doi:10.1002/pssa.19700010402.
[46] T.O. Mason, Electronic behavior and cationic defects in cubic transition metal oxides, Phys. BC. 150 (1988) 37–43. doi:10.1016/0378-4363(88)90102-7.
[47] A. Rousset, C. Tenailleau, P. Dufour, H. Bordeneuve, I. Pasquet, S. Guillemet-Fritsch, V. Poulain, S. Schuurman, Electrical Properties of $Mn_{3-x}Co_xO_4$ ($0 \le x \le 3$) Ceramics: An Interesting System for Negative Temperature Coefficient Thermistors, Int. J. Appl. Ceram. Technol. 10 (2013) 175–185. doi:10.1111/j.1744-7402.2011.02723.x.
[48] Y. Liu, J.W. Fergus, K. Wang, C.D. Cruz, Crystal Structure, Chemical Stabilities and Electrical Conductivity of Fe-Doped Manganese Cobalt Spinel Oxides for SOFC Interconnect Coatings, J. Electrochem. Soc. 160 (2013) F1316–F1321. doi:10.1149/2.114311jes.
[49] D.R. Ou, M. Cheng, X.-L. Wang, Development of low-temperature sintered Mn–Co spinel coatings on Fe–Cr ferritic alloys for solid oxide fuel cell interconnect applications, J. Power Sources. 236 (2013) 200–206. doi:10.1016/j.jpowsour.2013.02.058.
[50] A.D. Sharma, J. Mukhopadhyay, R.N. Basu, Synthesis and Characterization of Nanocrystalline $MnCo_2O_{4-\delta}$ Spinel for Protective Coating Application in SOFC, ECS Trans. 35 (2011) 2509–2517. doi:10.1149/1.3570249.
[51] T. Kiefer, M. Zahid, F. Tietz, D. Stöver, H.R. Zerfass, Electrical conductivity and thermal expansion coefficientes of spinels in the series $MnCo_{2-x}Fe_xO_4$ for application as a protective

layer in SOFC, Proc. 26th Risö Int. Symp. Mater. Sci. Solid State Electrochem. (2005). http://juser.fz-juelich.de/record/49205 (accessed October 29, 2014).
[52] T. Brylewski, W. Kucza, A. Adamczyk, A. Kruk, M. Stygar, M. Bobruk, J. Dąbrowa, Microstructure and electrical properties of $Mn_{1+x}Co_{2-x}O_4$ ($0 \leq x \leq 1.5$) spinels synthesized using EDTA-gel processes, Ceram. Int. 40 (2014) 13873–13882. doi:10.1016/j.ceramint.2014.05.106.
[53] A. Petric, H. Ling, Electrical Conductivity and Thermal Expansion of Spinels at Elevated Temperatures, J. Am. Ceram. Soc. 90 (2007) 1515–1520. doi:10.1111/j.1551-2916.2007.01522.x.
[54] M.Y. Yoon, E.J. Lee, R.H. Song, H.J. Hwang, Preparation and properties of a $MnCo_2O_4$ for ceramic interconnect of solid oxide fuel cell via glycine nitrate process, Met. Mater. Int. 17 (2011) 1039–1043. doi:10.1007/s12540-011-6025-5.
[55] K. Wang, Y. Liu, J.W. Fergus, Interactions Between SOFC Interconnect Coating Materials and Chromia, J. Am. Ceram. Soc. 94 (2011) 4490–4495. doi:10.1111/j.1551-2916.2011.04749.x.
[56] B.-K. Park, J.-W. Lee, S.-B. Lee, T.-H. Lim, S.-J. Park, C.-O. Park, R.-H. Song, Cu- and Ni-doped $Mn_{1.5}Co_{1.5}O_4$ spinel coatings on metallic interconnects for solid oxide fuel cells, Int. J. Hydrog. Energy. 38 (2013) 12043–12050. doi:10.1016/j.ijhydene.2013.07.025.
[57] V. Miguel-Pérez, A. Martínez-Amesti, M.L. Nó, A. Larrañaga, M.I. Arriortua, The effect of doping $(Mn,B)_3O_4$ materials as protective layers in different metallic interconnects for Solid Oxide Fuel Cells, J. Power Sources. 243 (2013) 419–430. doi:10.1016/j.jpowsour.2013.05.109.
[58] A. Masi, M. Bellusci, S.J. McPhail, F. Padella, P. Reale, J.-E. Hong, R. Steinberger-Wilckens, M. Carlini, The effect of chemical composition on high temperature behaviour of Fe and Cu doped Mn-Co spinels, Ceram. Int. 43 (2017) 2829–2835. doi:10.1016/j.ceramint.2016.11.135.
[59] Y. Xu, Z. Wen, S. Wang, T. Wen, Cu doped Mn–Co spinel protective coating on ferritic stainless steels for SOFC interconnect applications, Solid State Ion. 192 (2011) 561–564. doi:10.1016/j.ssi.2010.05.052.
[60] J. Xiao, W. Zhang, C. Xiong, B. Chi, J. Pu, L. Jian, Oxidation behavior of Cu-doped $MnCo_2O_4$ spinel coating on ferritic stainless steels for solid oxide fuel cell interconnects, Int. J. Hydrog. Energy. (2016). doi:10.1016/j.ijhydene.2016.03.051.
[61] A. Masi, M. Bellusci, S.J. McPhail, F. Padella, P. Reale, J.-E. Hong, R. Steinberger-Wilckens, M. Carlini, Cu-Mn-Co oxides as protective materials in SOFC technology: The effect of chemical composition on mechanochemical synthesis, sintering behaviour, thermal expansion and electrical conductivity, J. Eur. Ceram. Soc. 37 (2017) 661–669. doi:10.1016/j.jeurceramsoc.2016.09.025.
[62] J.C.W. Mah, A. Muchtar, M.R. Somalu, M.J. Ghazali, J. Raharjo, Formation of sol–gel derived (Cu,Mn,Co)3O4 spinel and its electrical properties, Ceram. Int. 43 (2017) 7641–7646. doi:10.1016/j.ceramint.2017.03.060.
[63] M.E. dos Santos, R. Aparecido Ferreira, P. Noronha Lisboa-Filho, O. Peña, Cation distribution and magnetic characterization of the multiferroic cobalt manganese $Co_2MnO_4$ spinel doped with bismuth, J. Magn. Magn. Mater. 329 (2013) 53–58. doi:10.1016/j.jmmm.2012.09.070.
[64] T. Mokkelbost, Ø. Andersen, R.A. Strøm, K. Wiik, T. Grande, M.-A. Einarsrud, High-Temperature Proton-Conducting $LaNbO_4$-Based Materials: Powder Synthesis by Spray Pyrolysis, J. Am. Ceram. Soc. 90 (2007) 3395–3400. doi:10.1111/j.1551-2916.2007.01904.x.
[65] E. Aukrust, A. Muan, Phase Relations in the System Cobalt Oxide–Manganese Oxide in Air, J. Am. Ceram. Soc. 46 (1963) 511–511. doi:10.1111/j.1151-2916.1963.tb13790.x.
[66] D. a. G. Bruggeman, Berechnung verschiedener physikalischer Konstanten von heterogenen Substanzen. I. Dielektrizitätskonstanten und Leitfähigkeiten der Mischkörper aus isotropen Substanzen, Ann. Phys. 416 (1935) 636–664. doi:10.1002/andp.19354160705.
[67] R. Landauer, Electrical conductivity in inhomogeneous media, in: AIP Conf. Proc., AIP Publishing, 1978: pp. 2–45. doi:10.1063/1.31150.
[68] N. Tsuda, K. Nasu, A. Fujimori, K. Siratori, Electronic Conduction in Oxides, Springer Berlin Heidelberg, Berlin, Heidelberg, 2000. http://link.springer.com/10.1007/978-3-662-04011-9 (accessed June 19, 2015).
[69] G.V. Bazuev, A.V. Korolyov, Magnetic behavior of $MnCo_2O_{4+\delta}$ spinel obtained by thermal decomposition of binary oxalates, J. Magn. Magn. Mater. 320 (2008) 2262–2268. doi:10.1016/j.jmmm.2008.04.123.

[70] H.S.C. O'Neill, A. Navrotsky, Simple spinels; crystallographic parameters, cation radii, lattice energies, and cation distribution, Am. Mineral. 68 (1983) 181–194.
[71] R.J. Hill, J.R. Craig, G.V. Gibbs, Systematics of the spinel structure type, Phys. Chem. Miner. 4 (1979) 317–339. doi:10.1007/BF00307535.
[72] R.D. Shannon, Revised effective ionic radii and systematic studies of interatomic distances in halides and chalcogenides, Acta Crystallogr. Sect. A. 32 (1976) 751–767. doi:10.1107/S0567739476001551.
[73] L.V. Gambino, A.B. Freeman, N.J. Magdefrau, M. Aindow, ALCHEMI studies of site occupancies in Cr-, Ni-, and Fe-substituted manganese cobaltite spinels, J. Mater. Sci. (2015) 1–13. doi:10.1007/s10853-015-9307-3.
[74] D.S. McClure, The distribution of transition metal cations in spinels, J. Phys. Chem. Solids. 3 (1957) 311–317. doi:10.1016/0022-3697(57)90034-3.
[75] V. a. M. Brabers, F. van Setten, X-ray photoelectron spectroscopy study of the ionic configuration of the spinel $CuMnCoO_4$, J. Phys. Appl. Phys. 16 (1983) L169. doi:10.1088/0022-3727/16/9/001.
[76] P.A. Wright, S. Natarajan, J.M. Thomas, P.L. Gai-Boyes, Mixed-metal amorphous and spinel phase oxidation catalysts: characterization by X-ray diffraction, X-ray absorption, electron microscopy, and catalytic studies of systems containing copper, cobalt, and manganese, Chem. Mater. 4 (1992) 1053–1065. doi:10.1021/cm00023a024.
[77] B.L. Yang, S.F. Chan, W.S. Chang, Y.Z. Chen, Surface enrichment in mixed oxides of Cu, Co, and Mn, and its effect on CO oxidation, J. Catal. 130 (1991) 52–61. doi:10.1016/0021-9517(91)90091-H.
[78] X. Chen, P. Hou, C. Jacobson, S. Visco, L. Dejonghe, Protective coating on stainless steel interconnect for SOFCs: oxidation kinetics and electrical properties, Solid State Ion. 176 (2005) 425–433. doi:10.1016/j.ssi.2004.10.004.
[79] E. Cuciureanu, S. Istrate, N. Rezlescu, On the Time Variation of the Conductivity in Nickel and Copper Ferrites, Phys. Status Solidi A. 6 (1971) K37–K38. doi:10.1002/pssa.2210060149.
[80] N. Rezlescu, E. Cuciureanu, C. Ioan, E. Luca, Time variation of the electrical conductivity in spinel ferrites, Phys. Status Solidi A. 11 (1972) 351–359. doi:10.1002/pssa.2210110137.
[81] W.A. Groen, C. Metzmacher, P. Huppertz, S. Schuurman, Aging of NTC Ceramics in the System Mn-Ni-Fe-O, J. Electroceramics. 7 (2001) 77–87. doi:10.1023/B:JECR.0000027947.28060.33.
[82] A.D.D. Broemme, Physico-chemical investigations on Co-Mn-oxide spinels. PhD Thesis., Technische Universiteit Eindhoven, 1990. http://adsabs.harvard.edu/abs/1990PhDT.....29B (accessed February 28, 2016).
[83] G.G. Xia, Z.G. Yang, J. Stevenson, Manganese-Cobalt Spinel Oxides as Surface Modifiers for Stainless Steel Interconnects of Solid Oxide Fuel Cells, ECS Trans. 1 (2006) 325–332. doi:10.1149/1.2215566.
[84] J. Xiao, W. Zhang, C. Xiong, B. Chi, J. Pu, L. Jian, Oxidation of $MnCu_{0.5}Co_{1.5}O_4$ spinel coated SUS430 alloy interconnect in anode and cathode atmospheres for intermediate temperature solid oxide fuel cell, Int. J. Hydrog. Energy. 40 (2015) 1868–1876. doi:10.1016/j.ijhydene.2014.11.124.
[85] V.A.M. Brabers, A.D.D. Broemme, Low-spin-high-spin transition in the $Co_3O_4$ spinel, J. Magn. Magn. Mater. 104–107, Part 1 (1992) 405–406. doi:10.1016/0304-8853(92)90853-G.

# Supplementary material

Thermogravimetric analysis (TGA) was performed using TG 439 Thermo-Microbalance from Netzsch. The mass change of the sample is measured against a reference ($Al_2O_3$ powder) and in principle, this should eliminate any buoyancy effects. This means that a measurement with empty crucibles should result in no recordable mass change with change in temperature. In practice, this was not the case. Figure S1 shows the measurement with empty crucibles between room temperature and 800 °C, with heating and cooling rates of 10 K/min (first cycle) and 1 K/min (second cycle). All the results presented in the paper were corrected against this background measurement. Figure S1 also shows the measurement results of the $MnCo_2O_4$ powder before correction for background was made. It may be noticed that the mass change of the sample between 300-500 °C is significantly larger than the mass change in the background measurement. Furthermore, the characteristic peak in mass change in this temperature interval is reproduced with different samples and using different heating/cooling rates.

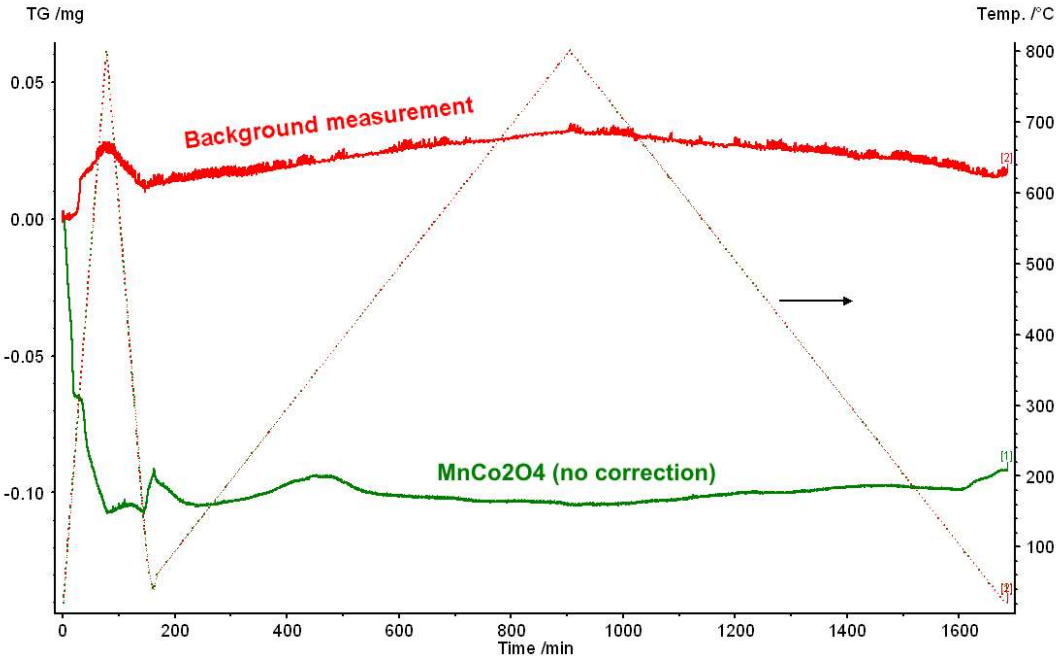


**Figure S1**. Background measurement for thermogravimetrical analysis made with empty alumina crucibles and original measurement data for $MnCo_2O_4$ before applying the background correction.

To improve readability of the TGA results, the inherent noise of the measurement was reduced by fitting the experimental data to a polynomial curve. This was performed using the negative exponential function in Sigmaplot 13.0. The polynomial degree was set to 1 or 2 based on visual evaluation of best fit to original data. Figure S2 shows an example of the original data and polynomial fit for the $MnCo_2O_4$ material.

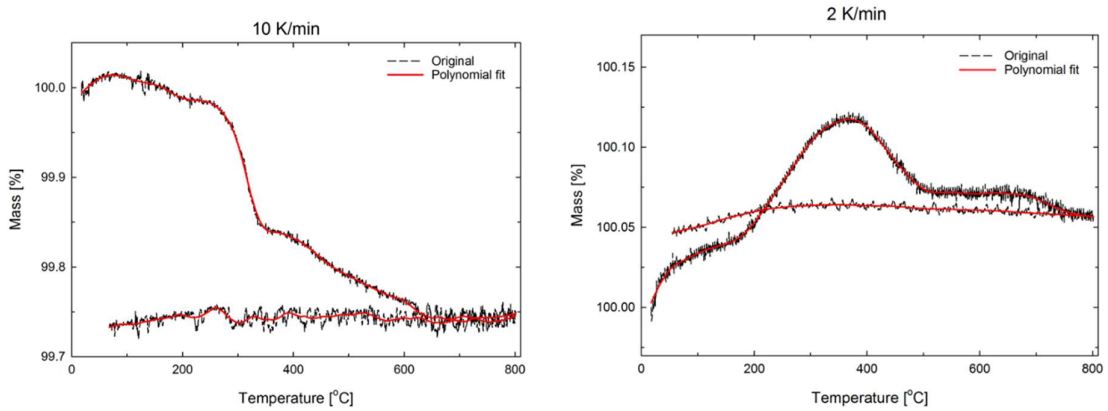


**Figure S2**. Polynomial fit of the experimental thermogravimetric analysis data of $MnCo_2O_4$.

Figure S3 shows X-ray diffraction patterns for spinel ceramics in air at 1100 °C (5h) + 800 °C (12 h). These results were used to determine the lattice parameters, as described in the paper.

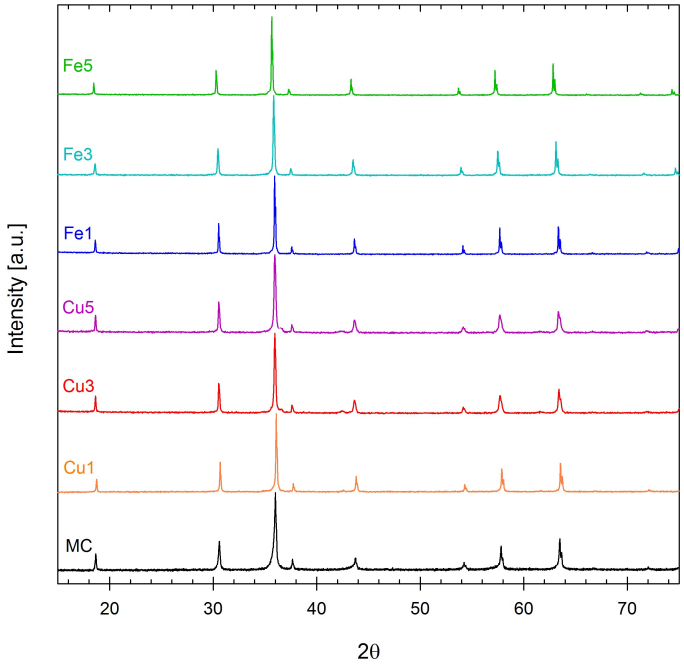


**Figure S3**. X-ray diffractograms of spinel ceramics sintered in air at 1100 °C (5h) + 800 °C (12 h).

Only the heating parts of the dilatometer measurements were shown in the paper. Figure S4 shows both the heating and cooling curve for the Fe1 composition, measured between room temperature and 1000 °C. A significant negative hysteresis is observed between the heating and cooling segments. Figure S4 also shows a new sample of the same material measured between room temperature and 800 °C. The hysteresis is seen to be considerably reduced, although not completely eliminated when the measurement is reversed at lower temperature. Based on this, the large hysteresis when the measurement is reversed at 1000 °C was attributed to creep or the onset of Co-reduction in the materials.

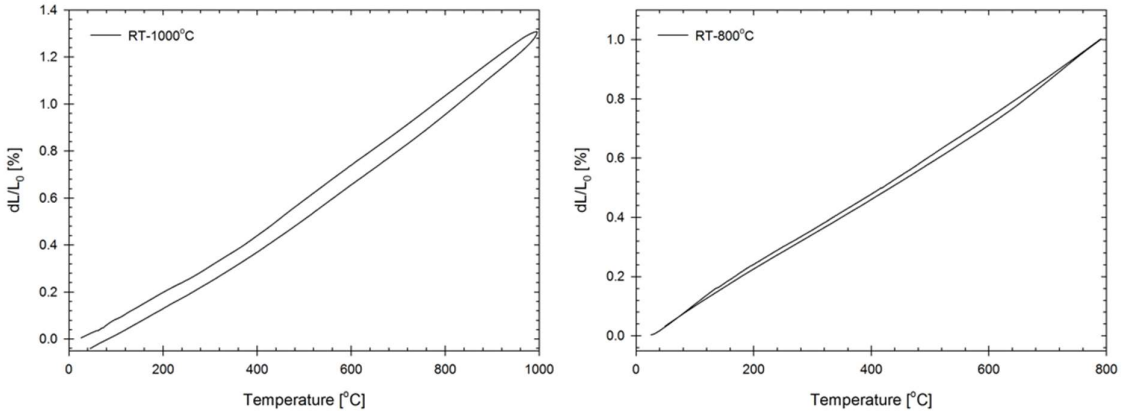


**Figure S4.** Heating and cooling curve for the thermal expansion data of the Fe1 material. Measurement reversed at 1000 °C (left) and 800 °C (right).

A hysteresis in the electrical conductivity of the $MnCo_2O_4$ material was observed between heating and cooling (Figure 6 in the paper). Figure S5 shows the electrical conductivity for two different samples of the Cu1 material. The sample with 60 % density displays hysteresis in electrical conductivity between heating and cooling (Fig. 6b). The sample with 84 % density does not display any hysteresis (Fig. 6a). The reason for the hysteresis in electrical conductivity is discussed in the paper.

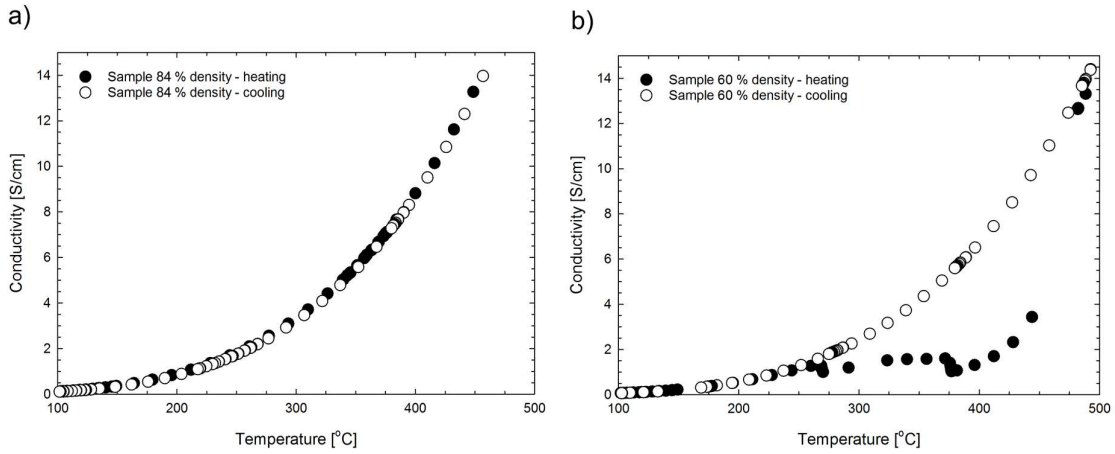


**Figure S5**. Electrical conductivity of Cu1 measured during heating and cooling in air . Results for two samples with different sample density, (a) 84 % and (b) 60 %. The results are excerpts from measurements between room temperature and 1000 °C and are corrected for sample porosity.

Thermogravimetric analysis of MC, Fe3 and Cu3 powders is shown in Figure S6 and S7. The initial mass loss below 200 °C may be attributed to evaporation of adsorbed moisture. Upon further heating, all of the samples gain mass up to ca. 400 °C, before the mass decreases again. The results are discussed in the paper.

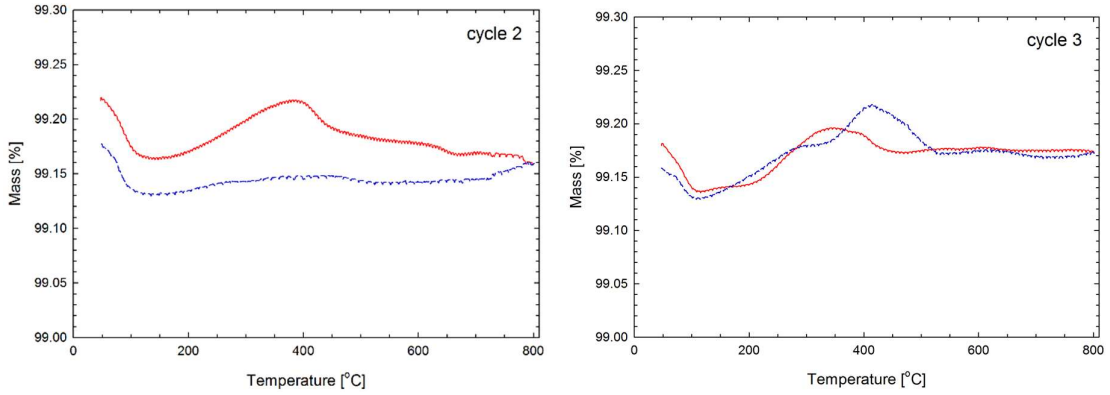


**Figure S6**. Thermogravimetric analysis of MC powder (obtained from a crushed ceramic sintered 1100 °C+ 800 °C) showing relative weight change during heating in air for two consecutive cycles. Heating and cooling rate 2 °C/min. Red solid lines = heating, blue stippled lines = cooling

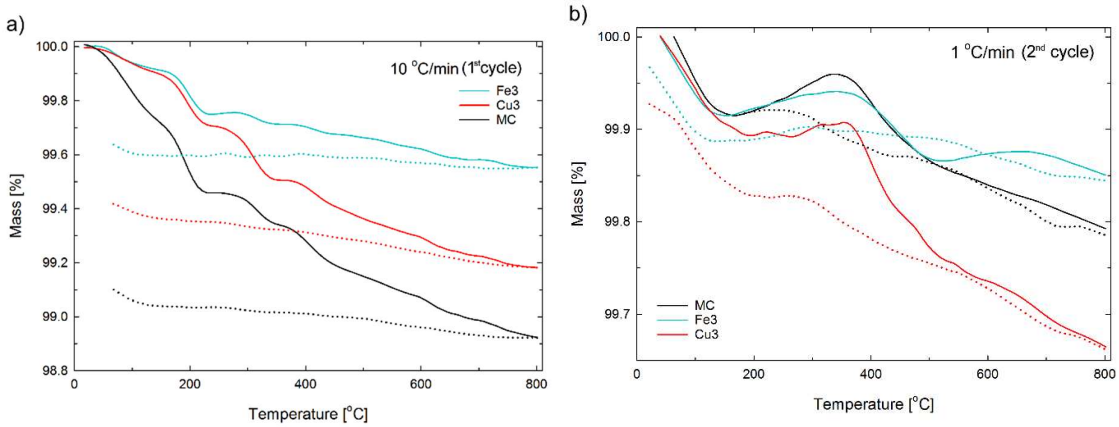


**Figure S7**. Thermogravimetric analysis of MC, Fe3 and Cu3 powders (calcined 650 °C) showing relative weight change during heating in air. Solid lines = heating, stippled lines = cooling. (a) heating and cooling rate 10 °C/min, (b) second cycle of samples in a) with heating and cooling rate 1 °C/min. The curves have been shifted to start at 100 % mass.